Influence of the gap size on the response of a single-degree-of-freedom vibro-impact system with two-sided constraints: experimental tests and numerical modeling

Giulia Stefani[a,*], Maurizio De Angelis[a], Ugo Andreaus[a]

[a]*Department of Structural and Geotechnical Engineering, "Sapienza" University of Rome, Via Eudossiana 18, 00184 Rome, Italy*

Abstract

The large displacements caused by strong earthquakes in base-isolated structures (building, bridges, strategic facilities, equipment, ...) can excessively deform or damage the isolation system or lead to pounding with surrounding moat walls or adjacent structures, if the available seismic gap is not sufficient. The acceleration spikes caused by the impact can damage the structure itself as well as sensitive equipment housed in it. A possible mitigation measure consists in the interposition of deformable shock absorbers (bumpers). In this paper, the influence of the gap amplitude on the experimental response of a single-degree-of-freedom oscillator, excited by a harmonic base acceleration and symmetrically constrained by two unilateral deformable and dissipative bumpers, is investigated. The parametric investigation considered both positive, null and negative gaps. Particular attention is paid to the study of the effect, on the system response, of the transition from positive to small negative gaps and of excessive negative gaps. Secondary resonances in the low frequency range, associated with the occurrence of multiple impacts, were observed for small positive gaps. Finally, the experimental results were reproduced, in a sufficiently accurate manner, using a suitable numerical model, whose parameters were identified based on the experimental data.

Keywords: Small and negative gaps, Primary and secondary resonances, Right and left hysteresis, Multiple impacts, Shaking table tests, Numerical model

1. Introduction

The impact phenomenon is ubiquitous in many (biomedical, mechanical, civil,) engineering applications involving mechanical components or structures repeatedly colliding with one another or with obstacles. Some examples are represented by the capsule systems used in clinic endoscopy to inspect the surface lining of the intestine in the human body [1–6] and the drilling rig used in the oil and gas industry for creation of the wells [7–13]. In the context of civil engineering, base isolation represents one of the most applied passive control strategies to mitigate the dynamic response of both new and existing structures [14–17], bridges [18–20], strategic facilities [21, 22], nonstructural elements and equipment [23–27]. The aim of base isolation is to uncouple the motion of the structure from that of the ground by introducing some type of support that isolates it from the shaking ground, thus limiting the energy input into the system and protecting it from damaging. The flexibility introduced by base isolation increases the fundamental vibration period of the structure. The occurrence of exceptional loads, like strong earthquakes, can produce large horizontal displacements in base-isolated structures, concentrated in the isolation system, which can damage the isolation system itself or can lead to pounding with the surrounding moat walls or adjacent structures [28–30], if the available seismic gap is not sufficient. A possible mitigation measure consists in the interposition of deformable shock absorbers (bumpers) [31–33]. On the one hand, the introduction of the bumpers limits the displacement of the structure; on the other, the possible occurrence of the impact with the bumpers can produce acceleration spikes which can be detrimental, not only for the structure itself, but also for any sensitive equipment housed in it. Furthermore, the occurrence of impact can excessively deform the bumpers. In order to limit the response of the base-isolated system, so as to avoid the damage of the isolation system, also other types of control systems can be implemented [34–37].

The nonsmooth dynamics of systems with one-sided or two-sided constraints, the types of impact motion, attractors and bifurcations, have been the subject of several scientific works, of both numerical and experimental nature [38–53]. The effect of the introduction of the obstacle on the system response depends on several factors, including the mechanical properties of the bumpers and the distance between them and the structure (gap). As concerns the influence of the gap size, few works can be found in Literature, usually dealing with positive gaps. In these works the response is found to decreases as the gap increases [31, 54–57]. Very small seismic gaps, in combination with strong ground excitation, can lead to relatively milder consequences from pounding, not allowing the structure to develop high velocities before the impact [56, 57]. According to Jankowski et al. [18] the optimal gap size to reduce the response is either a very small one or large enough to avoid

*Corresponding author

Email addresses: giulia.stefani@uniroma1.it (Giulia Stefani), maurizio.deangelis@uniroma1.it (Maurizio De Angelis), ugo.andreaus@uniroma1.it (Ugo Andreaus)

collisions. The zero-gap configuration was recommended by Aguiar and Weber [58], since it allows to maximize the impact force in a vibro-impact system without the occurrence of nonlinear jumps. Even less are the works that deal with negative gaps, which cause an initial pre-stress/pre-strain state in the bumpers. Relatively simpler dynamic responses of a two-degree-of-freedom periodically-forced system are found in [59] if the constraints are initially prepressed. The effect of the introduction of a prepressing constraint in a capsule system was highlighted in [5].

The practical problem of excessive displacements in base-isolated structures inspired several works of the authors, of both numerical and experimental nature, in which a single-degree-of-freedom oscillator, impacting against two deformable and dissipative bumpers, was considered [60–68]. Some of the scenarios which can occur in the experimental nonlinear non-smooth response of the system were identified and described in [68]. These scenarios were also reproduced with a suitable numerical model. Further numerical investigations highlighted the existence of gradually more complex and varied behaviors, that could be observed for values of the gap smaller than those considered in the experimental laboratory campaign [68]. Furthermore, the combination of small gaps with quite deformable bumpers appeared to be a good choice which allows to realize, compared to the free flight condition, a reduction of both accelerations and displacements or a good compromise between reduction of displacements and limited increase in accelerations [64].

Based on these preliminary results, a new laboratory campaign was designed and conducted to investigate, in particular, small positive, null and negative values of the gap and to validate the numerical predictions. The experimental investigation of small positive, null and negative gaps represent an element of novelty of this laboratory campaign. Furthermore, compared to the previous experimental investigations made by the authors, impact load cells were installed between the mass and the bumpers, to directly measure the contact force during the impact phases. In this paper some results of the new laboratory campaign will be presented and discussed. The attention is focused of the influence of the gap amplitude on the system (mass and bumpers) response, especially when passing from small positive to small negative gaps and when the negative gap exceeds a certain threshold value. For small positive gaps, secondary resonances in the low frequency range were observed and the response of the system at these resonances was investigate. Based on the experimental results, the parameters of a relatively simple numerical model were identified in order to reproduce the experimental outcomes. Although several scientific works deal with the problem of impact, there are not many studies that address, in such a systematic way, the study of the influence of the gap on the dynamic response of the system, extending the investigations also to small positive, null and negative gaps.

The paper is organized as follows. The experimental setup is introduced in Sect. 2; some experimental results are presented and discussed in Sect. 3; the transition from positive to small negative gaps, the effect of excessive negative gaps and the characteristics of the system's response at the secondary resonances are investigated in Sect. 4; the numerical model and the comparison between experimental and numerical results are presented in Sect. 5; finally, concluding remarks and future developments of the work are given in Sect. 6.

2. Experimental setup and performed tests

The experimental setup, shown in Fig. 1, consists of a rigid body (mass $M = 550$ kg), an elastomeric high damping rubber bearing (HDRB) isolator (damper), and two elastomeric shock absorbers (bumpers), symmetrically mounted on steel moat walls, denoted as right (B_R) and left (B_L) bumper respectively. The experimental tests investigated two configurations, namely with and without bumpers (the latter will be referred to as free flight condition), under the same base excitation. To study the response of the system in the presence of obstacles, an elastomeric bumper with D-shape hollow section, in the following denoted as B2, was tested (see the photograph in the bottom right corner of Fig. 1).

By adjusting the screws behind the plates on which the bumpers are mounted, the distance between the mass and the bumpers (gap) was varied. The gaps considered in the experimental tests were denoted as: G∞, G30, G16, G10, G4, G0, G-1, G-2, G-10, where the number, expressed in mm, represents the nominal amplitude of the total gap G, defined as the sum of the right and left gaps and G∞ indicates the free flight condition. It is worth noting that in the experimental tests, as far as possible, an attempt has been made to achieve a gap equal to the nominal value. The negative gaps (G-1, G-2, G-10) were realized by initially compressing the bumpers against the mass, leading to an initial pre-stress/pre-strain state in the bumpers. The investigation of small positive, null and negative gaps represents one of the novelty elements of this laboratory campaign, compared to previous tests and works of the authors.

The experimental tests were carried out in the Materials and Structures Testing Laboratory of the Department of Structural and Geotechnical Engineering of "Sapienza" University of Rome, using a uni-axial shaking table Moog 1.50×1.50 m, managed by Moog Replication Software. The system was excited at the base by a step-wise forward and backward sine sweep in displacement control, in order to impose a given value of peak table acceleration, namely A = 0.05 g, where g is the gravity's acceleration, with a number of cycles n, in each sub-frequency range, such as to reach the steady state condition. For positive gaps ($G > 0$), the investigated frequency range was between 0.5 and 5 Hz, with frequency step $\Delta f = 0.1$ Hz and $n = 10$. For $G \leq 0$, the investigated frequency range was extended from 0.5 to 10 Hz, with frequency step $\Delta f = 0.1$ Hz and $n = 10$. In some cases, especially for small positive gaps (G10 and G4), in order to better capture the experimental response of the system in the low frequency range, the frequency step Δf and the number of cycles n were varied, depending on the performance of the shaking table, as it will be illustrated in more detail in Sect 4.3.

The measured quantities during the tests were the total accelerations and displacements of the mass and of the shaking table

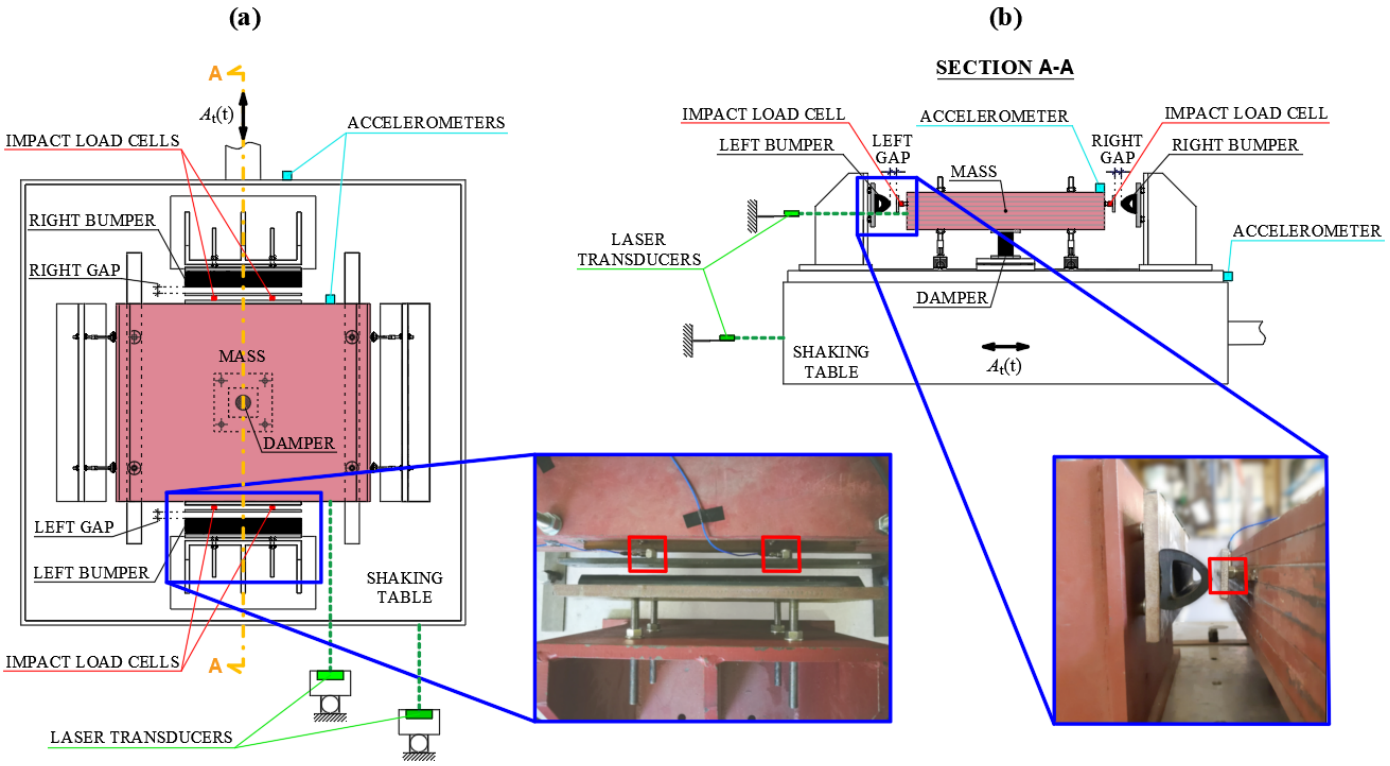

Figure 1: Experimental setup: **a** plan view and **b** side view with indication of the main components and sensors. The zoomed areas show two photographs with details of the impact load cells, enclosed by red squares.

and the contact forces between mass and bumpers. The accelerations were measured by accelerometers and the displacements by laser transducers (Fig. 1). The forces developed during the contact phases between mass and bumpers were measured by four impact load cells, symmetrically mounted on the mass, two on each side (see the two zoomed areas in Fig. 1). Between the impact load cells and the bumpers, steel plates were mounted to distribute the impact force. The use of impact load cells, in addition to the other sensors, represents another novelty element of this laboratory campaign, compared to previous tests and works of the authors.

3. Experimental Results

The total gap amplitude G influences the system response, as shown in Fig. 2, in terms of forward (red lines and dots) and backward (blue lines and dots) Pseudo-Resonance Curves (PRCs). Each PRC corresponds to an experimentally tested value of G. The size of the dots and the thickness of the lines decrease as G decreases. In Fig. 2a,b the green curves refer to the free flight condition (also referred to as G∞ in the legend).

The represented response quantities are the normalized excursion of the relative displacement of the mass η_d (Fig. 2a), the normalized excursion of the absolute acceleration of the mass η_a (Fig. 2b), the normalized maximum deformation η_j (Fig. 2c) and maximum contact force r_j (Fig. 2d) of the right ($\mathrm{B_R}$) and left ($\mathrm{B_L}$) bumpers respectively (j = R, L). These quantities are defined as follows:

$$\eta_\mathrm{d} = \frac{E_\mathrm{d}}{E_\mathrm{d0}} = \frac{u_\mathrm{max} - u_\mathrm{min}}{2u^*} \tag{1a}$$

$$\eta_\mathrm{a} = \frac{E_\mathrm{a}}{E_\mathrm{a0}} = \frac{a_\mathrm{max} - a_\mathrm{min}}{2a^*} \tag{1b}$$

$$\eta_j = \frac{u_{j,\mathrm{max}}}{u^*} \quad (j = \mathrm{R, L}) \tag{1c}$$

$$r_j = \frac{F_{j,\mathrm{max}}}{Mg} \quad (j = \mathrm{R, L}) \tag{1d}$$

In the first three cases (Eqs. 1a-c), the normalization was made with respect to the free flight resonance condition (u^* and a^* denote the maximum relative displacement and absolute acceleration of the mass in free flight resonance condition). As concerns the contact force F_j (j = R, L), it is normalized with respect to the weight Mg of the impacting mass (Eq. 1d).

From Fig. 2 it can be observed that, for G > 0, compared to the free flight condition (green curves), the hardening caused by the impact between the mass and the bumpers bends the PRCs to the right, causing the occurrence of jumps (represented with vertical arrows for G4), and thus of a *primary right hysteresis* (highlighted in yellow). Referring to the primary resonance condition, it can be observed that, progressively approaching the bumpers to the mass, that is decreasing G, the movement of the mass is increasingly limited and, consequently, the maximum value of η_d decreases (Fig. 2a). On the other hand, the maximum acceleration, after an initial increase, starts to decrease (Fig. 2b). Furthermore, as highlighted

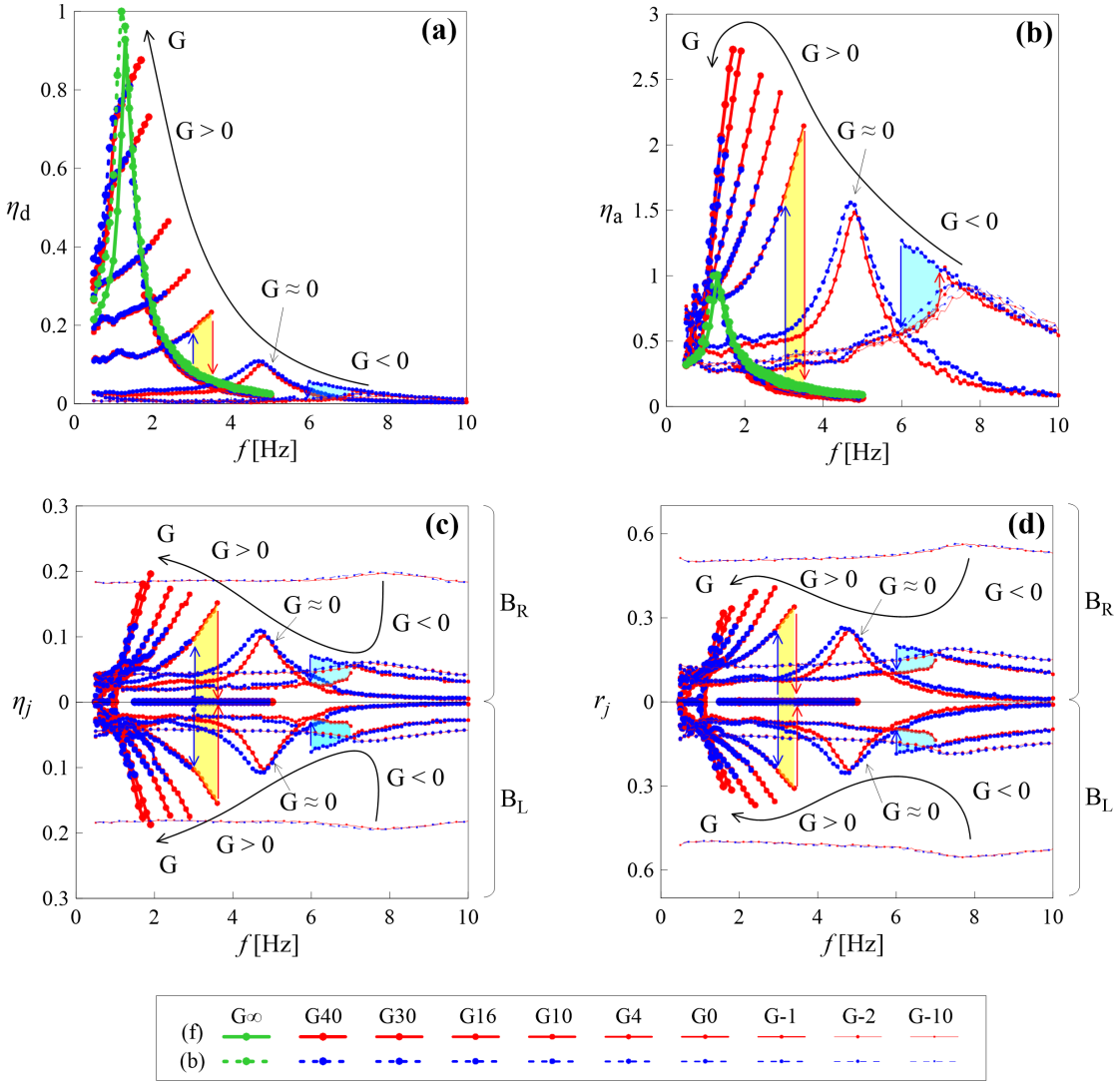

Figure 2: Forward (*red*) and backward (*blue*) PRCs of: **a** η_d; **b** η_a; **c** η_j (j = R, L) and **d** r_j (j = R, L) for different values of the total gap amplitude G. In **a** and **b**, the free flight condition (G∞) is represented with green curves.

by previous numerical investigations [68], for quite small gaps (G10 and G4) secondary resonances in the low frequency range were observed, and the number of secondary resonances was found to increase decreasing G. As concerns the two bumpers (Figs. 2c,d), it can be observed that the PRCs of the normalized deformation η_j and contact force r_j corresponding to the to bumpers (B_R, above the frequency axis and B_L, below the frequency axis) are qualitative similar to each other, due to the mostly symmetric behavior of the studied system. The trends of both the deformation (Fig. 2c) and the contact force (Fig. 2d) for decreasing positive gaps are similar to that of the acceleration of the mass (Fig. 2b). The jumps, the right hysteresis and the secondary resonances, are still visible also in these curves. Compared to the PRCs of η_d and η_a, for G > 0, the PRCs of η_j and r_j (j = R, L) are zero at the frequency values for which the impact does not occur.

The situation returns to be smooth for bumpers initially more or less in contact with the mass (G ≃ 0), with the forward and the backward PRCs, of both η_d, η_a, η_j and r_j (j = R, L) substantially overlapped, the resonance shifted to higher frequencies (about 4.8 Hz) and without jumps or hysteresis. As concerns the bumpers, since now impact occurs for each frequency value and consequently, the PRCs of η_j and r_j (j = R, L) are always different from zero.

For small negative gaps (G-1), obtained by initially slightly compressing the bumpers against the mass, the PRCs bend to the left, due to a softening-like behavior, showing jumps (represented with vertical arrows) and a *primary left hysteresis* (highlighted in cyan). The left hysteresis is observed in the PRCs of both η_d, η_a, η_j and r_j (j = R, L). The initial pre-stress/pre-strain state of the bumpers, resulting from the negative gaps, causes an offset of the PRCs of η_j (Fig. 2c) and r_j (Fig. 2d) (j = R, L) from the frequency axis. Consequently, as in the G≃ 0 case, these curves are always different from zero.

By further compressing the bumpers against the mass (G-2 and G-10), the PRCs are no longer bent, show neither jumps

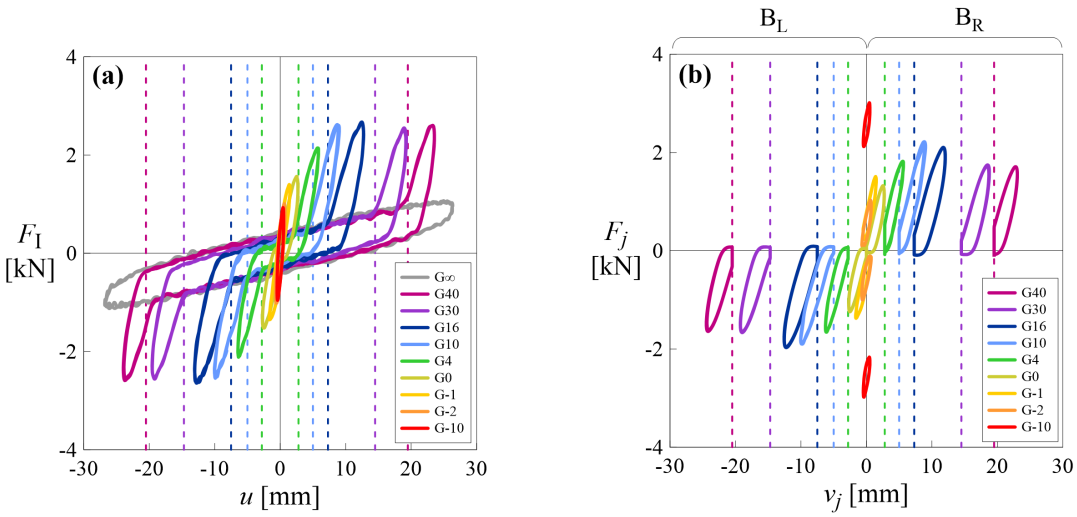

Figure 3: Force-displacement cycles in steady-state primary resonance condition corresponding to the investigated values of the total gap G: **a** mass; **b** bumpers.

nor hysteresis and the resonance is shifted to higher frequencies (about 7.5 Hz). Furthermore, while the PRCs of η_d and η_a corresponding to these two values of the gap are substantially overlapped, those of η_j and r_j (j = R, L) are similar but appear to be shifted with respect to each other, with the extent of the shift related to initial pre-stress/pre-strain state caused by the negative gap.

The effect of the gap amplitude G on the system response can be seen also from Fig. 3, in which the force-displacement cycles, in steady-state primary resonance condition, are represented, for both the mass (inertia force F_I vs. relative displacement u of the mass, Fig. 3a) and the two bumpers (contact force F_j vs. position v_j of the bumper, j = R, L, Fig. 3b). The position of the extremity of the bumper v_j (j = R, L) is measured from the side of the mass at time t = 0 s, as shown, in the schematic representations in Fig. 4, which refer to the right bumper (j = R). The position v_j is related to the deformation u_j, the latter used for the calculation of η_j, through the expression $v_j = u_j + G_{0j}$, where G_{0j} (j = R, L) represents the initial distance (gap) between the mass and the j-th bumper.

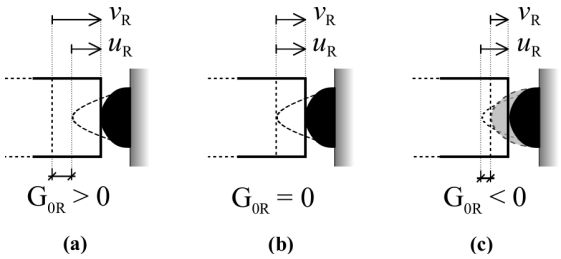

Figure 4: Graphical representation of the relationship between bumper's deformation u_j and position v_j for j = R (right bumper) and considering **a** positive, **b** null and **c** negative initial gaps. The dashed black lines represent the initial configuration of the system.

In Fig. 3 each color corresponds to a gap amplitude G and the vertical dashed lines represent the initial position of the bumpers for G > 0. Through these representations it is possible to see, in the same figure, the evolution of both the forces and the displacements with the amplitude of the gap. From Fig. 3a it is possible to observe both the increment of stiffness (hardening), which occurs when the mass impacts the bumper, for G ≥ 0, and the decrease in stiffness (softening) for small negative gaps (G-1, light orange curve). For negative gaps beyond a certain value (G-2 and G-10), the response of the mass does not vary significantly and the F_I-u cycles are substantially overlapped, though they are not quite the same, as it will be said in the following section. On the contrary, the pre-stress state induced in the bumpers by the negative gap causes the F_j-v_j (j = R, L) cycles to move away from the x-axis (Fig. 3b).

The behavior of the system for small positive, null and negative values of the gap will be discussed in more detail in the following Sect. 4.

4. Insights

In this section the attention is focused on the range of small positive, null and negative gaps. Starting from Fig. 5, in which only the PRCs corresponding to G4 (black lines and dots), G0 (red lines and dots), G-1 (blue lines and dots), G-2 (light green lines and dots) and G-10 (dark green lines and dots) are represented, three aspects will be further investigated, namely the transition from positive to negative small gaps (Sect. 4.1), the effect of excessive negative gaps on the mass and the bumpers' responses (Sect. 4.2), the characteristics of the system response for small positive gaps and in the low frequency range, where secondary resonances were observed (Sect. 4.3).

4.1. Transition from Positive to Negative Small Gaps

From Fig. 5 it can be observed that the transition from the hardening-like (black PRCs with *primary right hysteresis*) to the softening-like (blue PRCs with *primary left hysteresis*) behavior occurs moving from small positive to small negative values of the gap, passing through the approximately zero-gap configuration (G≃0, red PRCs). The force-displacement cycles

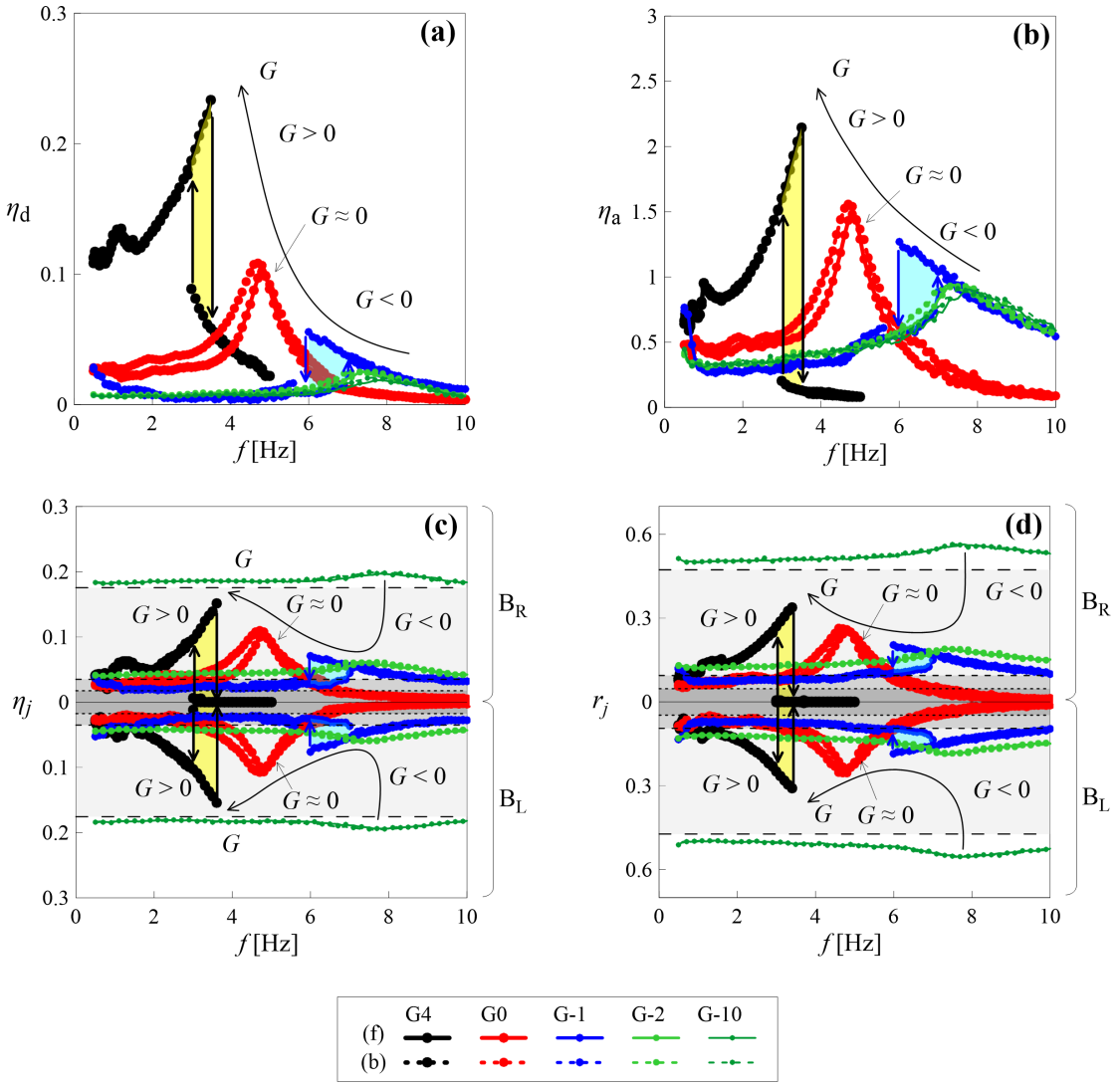

Figure 5: Forward (solid line) and backward (dashed line) PRCs of: **a** η_d; **b** η_a; **c** η_j (j = R, L) and **d** r_j (j = R, L) for G4 (black), G0 (red), G-1 (blue), G-2 (light green) and G-10 (dark green). In **a** and **b**, the PRCs corresponding to G-2 and G-10 are almost superimposed on each other. In **c** and **d**, the initial pre-strain/pre-stress states of the bumpers, resulting from the negative gap, are indicated by horizontal dashed lines and also highlighted with gray shaded areas which have, as baseline, the frequency axis.

in resonance condition, corresponding to the three gaps in the neighborhood of this transition (namely G4, G0 and G-1), are represented in Fig. 6. The top row refers to the mass (inertia force F_I vs. relative displacement u of the mass), the bottom row to the bumpers (contact force F_j vs. position v_j of the bumper, j = R, L). In the lower right corner of Figs. 6d-f

The first column on the left (Figs. 6a,d) corresponds to G4; at the *primary right hysteresis* (black PRCs in Fig. 5) two co-existing stable solutions are observed (Figs. 6a, 7a): one corresponding to large-amplitude oscillations with the occurrence of impact (forward sweep, solid red cycles) and the other to small-amplitude oscillations without impact (backward sweep, dashed blue cycles). In this frequency range, there would be also a third unstable solution, that could not be obtained experimentally. In Fig. 7a, in which the time history of the relative displacement u of the mass is depicted, both in the forward (solid red line) and in the backward (dashed blue line) sweeps, the horizontal dashed lines represent the initial gap and the vertical colored bands highlight the contact phases with each bumper (identified from the time histories of the contact forces). In the time interval between two consecutive colored bands, the mass is not in contact with either bumper (flight). The hardening-like behavior is related to the occurrence of the impact with one of the bumpers, which causes the adding of the resisting force exerted by the bumper to that of the damper.

For G $\simeq$ 0 (second column, Figs. 6b,e), the forward and backward cycles are more or less overlapping. In this condition, which is quite difficult to obtain experimentally, although no jumps or hysteresis occur in the PRCs (red PRCs in Fig. 5), the behavior of the system is still nonlinear [68]. The dissipative capability of the bumpers means that there is a short time interval in which the mass is not in contact with either bumper (Fig. 7b). This phase vanishes for purely elastic bumpers. Due to the small value of the relaxation time of the considered bumper

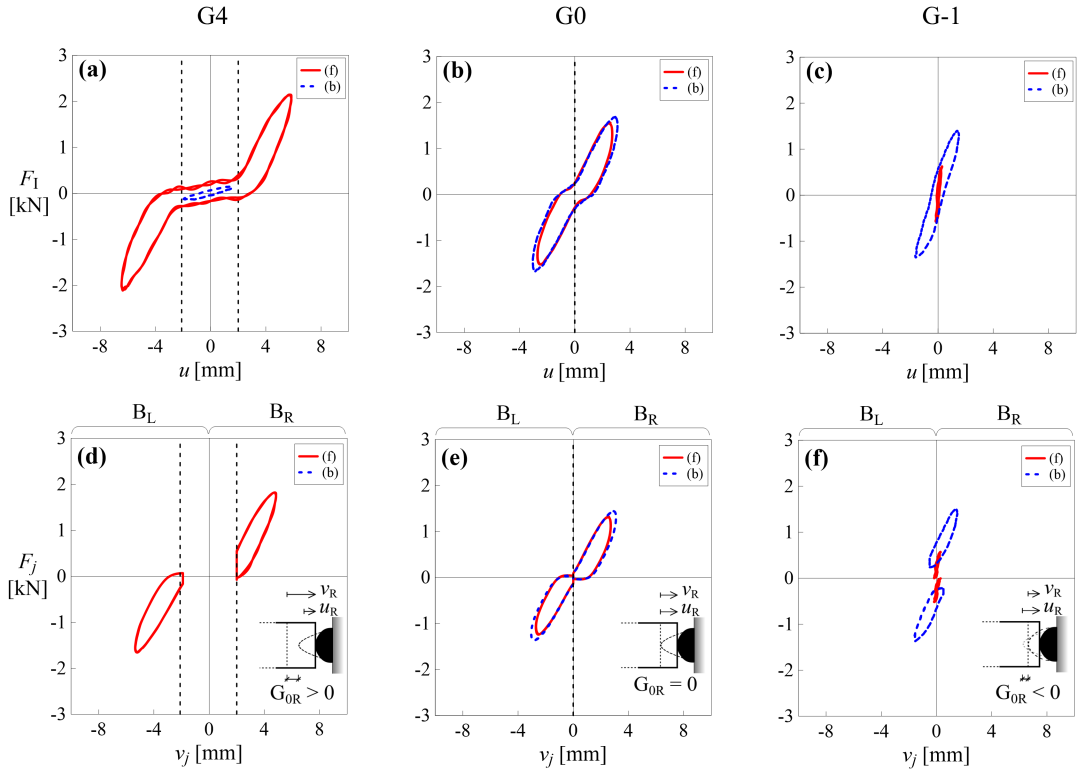

Figure 6: Force-displacement cycles in steady-state resonance condition corresponding to the forward (*red curve*) and the backward sweep (*blue curve*) for: G4, f = 3.4 Hz (*hardening*): **a** mass; **d** bumpers. G0, f = 4.8 Hz: **b** mass; **e** bumpers. G-1, f = 6 Hz (*softening*): **c** mass; **f** bumpers.

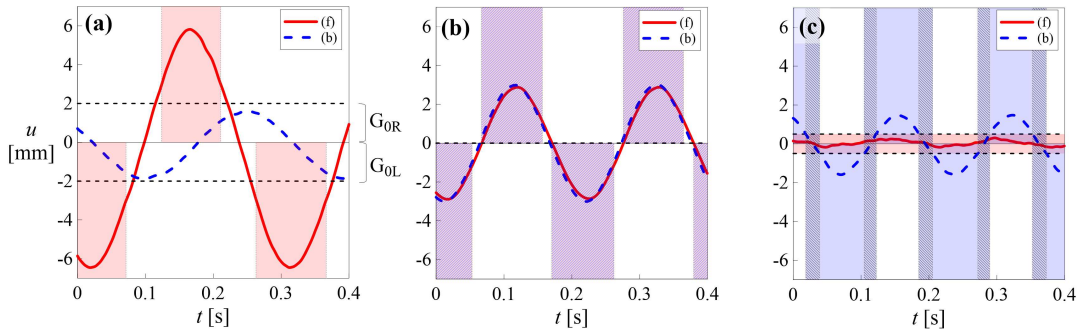

Figure 7: Time histories of the relative displacement u of the mass in steady-state condition: **a** G4, f = 3.4 Hz (*right hysteresis*); **b** G0, f = 4.8 Hz; **c** G-1, f = 6 Hz (*left hysteresis*). Red lines refer to the forward sweep, blue lines to the backward sweep. The horizontal dashed lines represent: **a**-**b** the initial gap; **c** the initial pre-strain of the bumpers. The contact phases with each bumper, identified from the time histories of the contact forces, are highlighted with vertical bands (red for the forward sweep, blue for the backward sweep).

(B2), the mass detaches from one bumper when the latter has recovered practically all its deformation and, right after, it impacts the other bumper, which, in the meantime, has already recovered its deformation. Consequently, also in this case, in addition to the nonlinearities associated with the behaviors of the damper and the bumpers, there is still the nonlinear contribution related to the occurrence of impact. By looking at Fig. 6b, it is possible to observe the increment of the stiffness associated with the occurrence of impact, while the central part of the cycle refers to the flight condition.

For small negative gaps (third column, Figs. 6c,f), a *primary left hysteresys*, associated with a softening-like behavior, was observed (blue PRCs in Fig. 5). In correspondence with this hysteresis, two stable solutions can be found (Figs. 6c, 7c). In particular:

- forward sweep (solid red cycles): the oscillations amplitude is always lower than the absolute value of the negative gap (represented in Fig. 7c with horizontal dashed lines). Consequently, the mass, during its motion, is always in contact with both bumpers and the resisting force is given by the sum of the forces exerted by the damper and the two bumpers.
- backward sweep (dashed blue cycles): as long as the amplitude of the displacement u of the mass is lower than the absolute value of the negative gap, the mass is in con-

tact with both bumpers (the corresponding time interval is highlighted in Fig. 7c with darker vertical bands), while when u exceeds this value, the mass detaches from one of the bumpers, remaining in contact with the other; this causes a reduction of the stiffness.

The initial pre-stress of the bumpers, resulting from the negative gap, causes an offset of the F_j-v_j (j = R, L) cycles from the x-axis (Fig. 6f). From the same figure, it is possible to observe also the increment of the stiffness when the mass is in contact with both bumpers (red cycles). As for the *primary right hysteresis*, also in this case, it was not possible to obtain the third unstable solution.

It is worth noting that the large-amplitude cycles, observed for G4 (forward sweep, Fig. 6a) and G-1 (backward sweep, Fig. 6c), are both characterized by nonlinearities associated with the unilateral constraint, as well as by the nonlinearities related to the behavior of the damper and the bumpers. The stiffness change is caused in the first case by the occurrence of impact between the mass and one of the two bumpers (*hardening*), and, in a dual manner, by the detachment with one of the bumpers in the second case (*softening*). In the other cases (small-amplitude cycles for G4 and G-1, the behavior of the system is still nonlinear, due to the behavior of the damper and the bumpers.

4.2. The Effect of Excessive Negative Gaps

From Fig. 5 it can also be observed that, for negative gap values greater than G-1 (G-2 and G-10), the PRCs (light green for G-2 and dark green for G-10) are no longer bent and show neither jumps nor hysteresis. For these values of the gap the mass, during its motion is always in contact with both bumpers. The PRCs of η_d (Fig. 5a) and η_a (Fig. 5b) are substantially superimposed, but they are not exactly the same, due to the nonlinear behavior of the damper and the bumpers. As concerns the bumpers, the PRCs of η_j (j = R, L) (Fig. 5c) and r_j (j = R, L) (Fig. 5d) have shifted with respect to each other. This shift is caused by the initial pre-stress/pre-strain state resulting from the negative gap, which has been highlighted in Figs. 5c,d with horizontal dashed lines and with gray shaded areas which have, as baseline, the frequency axis. Consequently, passing from G-2 to G-10, the PRCs of η_j and r_j (j = R, L) move away from the frequency axis. It is worth noting that, once the initial shift value has been removed, the resulting PRCs are substantially overlapped. Also in this case, these curves are not exactly the same, due to the nonlinear behavior of the damper and the bumpers.

Based on these considerations, it follows that, when the negative gap exceeds a certain value which, for the considered system (mass, damper and bumpers), is between G-1 and G-2, since the mass never detaches from the two bumpers, the resisting force is given by the sum of the forces exerted by the damper and the two bumpers. In this case, further increases in the absolute value of the negative gap, will only increase the initial pre-stress and pre-strain state of the bumpers, without affecting the mass response (Fig. 5).

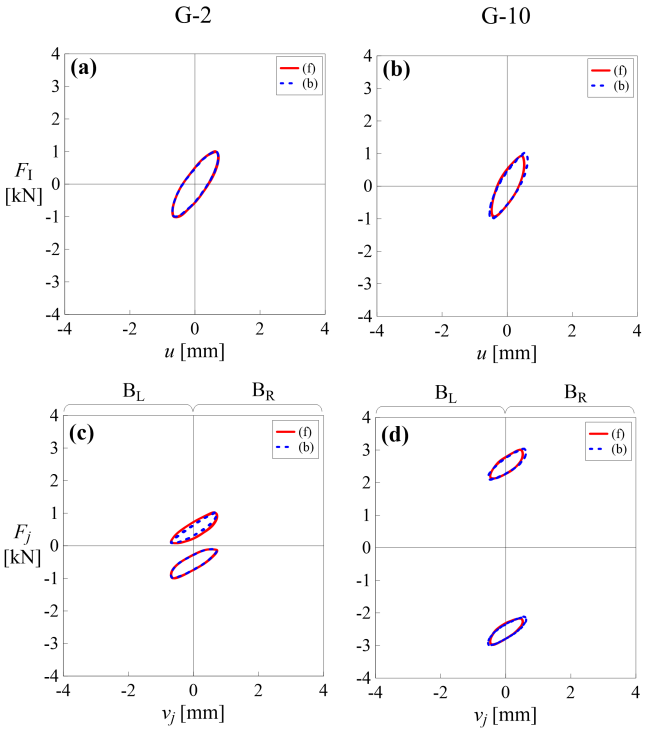

Figure 8: Force-displacement cycles in steady-state resonance condition corresponding to the forward (*red curve*) and the backward sweep (*blue curve*) for: G-2, f = 7.3 Hz: **a** mass; **c** bumpers. G-10, f = 7.6 Hz: **b** mass; **d** bumpers.

This can be seen also from Fig. 8, where the force-displacement cycles corresponding to G-2 (first column) and G-10 (second column), in steady-state resonance condition, are represented. As in Fig. 6, the top row refers to the mass (inertia force F_I vs. relative displacement u of the mass), and the bottom row to the bumpers (contact force F_j vs. position v_j of the bumper, j = R, L). It can be observed that, passing from G-2 to G-10, the F_I-u cycle (Figs. 8a,b) does not vary significantly. On the other hand, the consequent increase of the initial pre-stress state in the bumpers causes a gradually increasing distancing of the F_j-v_j (j = R, L) cycles (Figs. 8c,d).

4.3. Secondary Resonances

Previous numerical investigations by the authors [68] highlighted the existence of gradually more complex response scenarios, as the gap decreases, with the occurrence of the different types of secondary resonances in the low frequency range, not observed in previous experimental laboratory campaigns. The new experimental results, obtained considering smaller gaps compared to the previous tests, confirmed the numerical predictions. In fact, for quite small gaps (G10 and G4) secondary resonances in the low frequency range were observed and the number of resonances was found to increase decreasing the gap.

In order to experimentally describe these resonances in a sufficiently accurate manner, it was necessary to properly calibrate the input signal, as previously mentioned in Sect. 2. In particular, as concerns the case G4 (Fig. 9), three sine sweep (SSi, i = 1, 2, 3) signals were imposed to capture the secondary

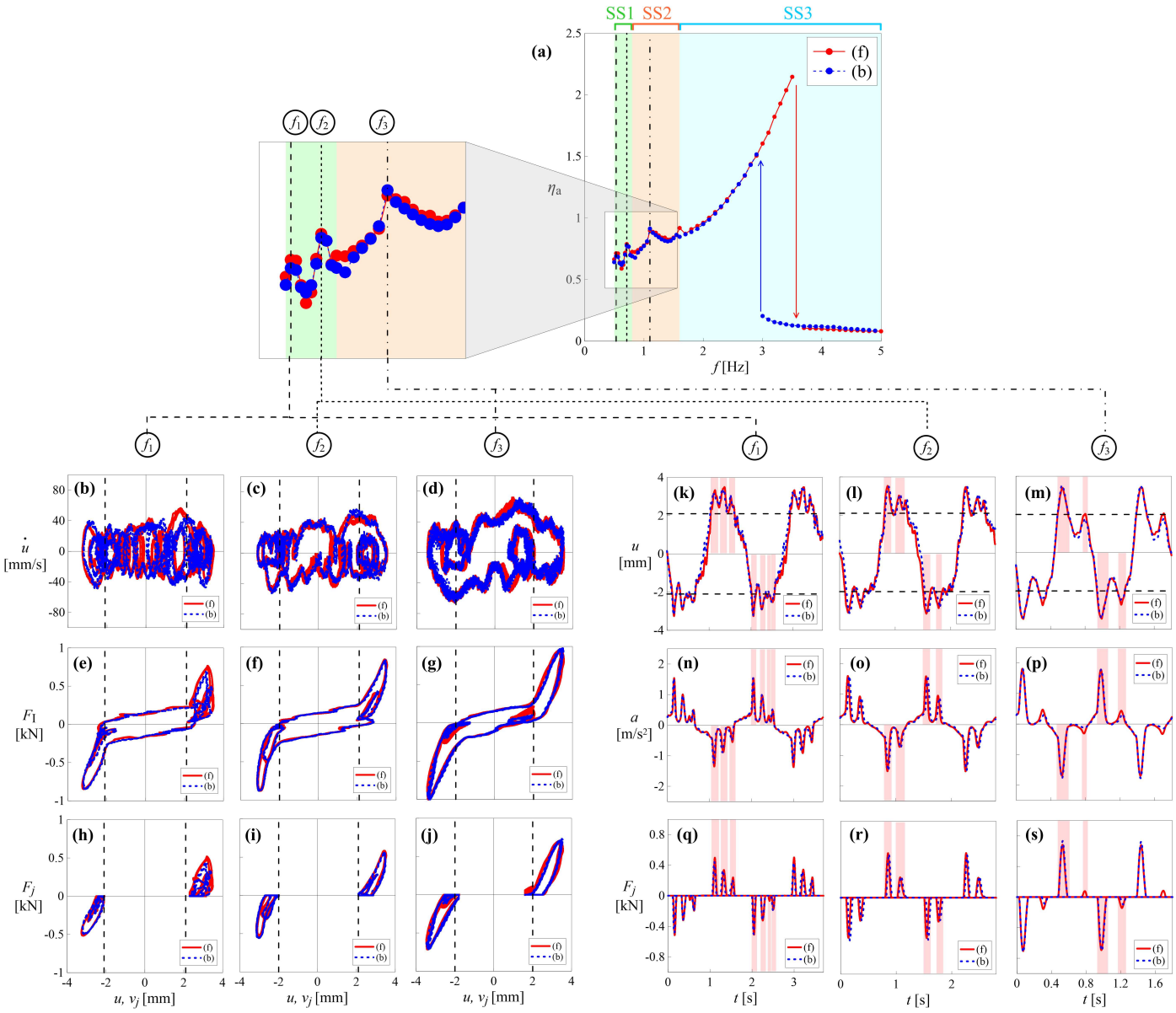

Figure 9: Secondary resonances in the low frequency range for G4: **a** PRC of η_a with indication of the different sweep frequency intervals (SSi, $i = 1, 2, 3$). The three vertical lines indicate the values of frequency corresponding to the observed secondary resonances ($f_1 = 0.53$ Hz, $f_2 = 0.71$ Hz, $f_3 = 1.1$ Hz). The other sub-figures represent, at these frequency values: **b**-**d** trajectories on the phase plane; **e**-**g** inertia force F_I vs. relative displacement u of the mass cycles; **h**-**j** contact force F_j vs. position v_j of the bumper cycles (j = R, L); **k**-**m** time history of the relative displacement u of the mass; **n**-**p** time history of the absolute acceleration a of the mass; **q**-**s**: time history of the contact forces F_j (j = R, L). In **b**-**m** the dashed black lines represent the initial gap. In **h**-**p** the vertical red bands represent the time intervals corresponding the contact phases with each bumper in one forcing cycle.

resonances, compatibly with the shaking table performances, namely:

- SS1 (highlighted with a vertical green band in Fig. 9a): sweep frequency range between 0.5 Hz and 0.8 Hz, with frequency step $\Delta f = 0.03$ Hz and $n = 20$ cycles in each sub-frequency range;

- SS2 (highlighted with a vertical orange band in Fig. 9a): sweep frequency range between 0.8 Hz and 1.6 Hz, with frequency step $\Delta f = 0.05$ Hz and $n = 30$ cycles in each sub-frequency range;

- SS3 (highlighted with a vertical light blue band in Fig. 9a): sweep frequency range between 0.5 Hz and 5 Hz, with frequency step $\Delta f = 0.1$ Hz and $n = 10$ cycles in each sub-frequency range.

By combining the results of these three tests, the PRCs corresponding to the gap G4, shown in Figs. 5 and 9a, were obtained. Three secondary resonances were observed at frequencies $f_1 = 0.53$ Hz, $f_2 = 0.71$ Hz, $f_3 = 1.1$ Hz (vertical dashed black lines in Fig. 9a). In correspondence with these resonances, it can be observed that forward and backward PRCs are substantially superimposed. The phase portraits, in steady

state condition, corresponding to the three resonances, are represented in Figs. 9b-d. The inertia force F_I vs. relative displacement u of the mass cycles are instead shown in Figs. 9e-g and the contact force F_j vs. position v_j of the bumper cycles (j = R, L) are represented in Figs. 9h-j. In the right part of Fig. 9, the time histories of the relative displacement u of the mass (Figs. 9k-m), the absolute acceleration a of the mass (Figs. 9n-p) and the contact forces F_j (j = R, L) (Figs. 9q-s), are illustrated. The solid red lines refer to the forward sweep, whereas the dashed blue lines correspond to the backward sweep.

The occurrence of internal loops in both the force-displacement cycles, rarely shown in literature, and the phase portraits, was observed in all three investigated cases. The existence of internal loops for small gap values was already predicted by the numerical model [68] and now confirmed experimentally. It can be observed that, for f_3 (Figs. 9d,g) these internal loops barely intersect the vertical dashed lines representing the position of the obstacles. Decreasing the frequency, that is passing from f_3 (Figs. 9d,g) to f_1 (Figs. 9b,e), these loops move outwards, intersecting the vertical lines in a more evident manner; furthermore, the number of internal loops increases. This is reflected in a number of impacts per forcing cycle, between the mass and each bumper, which increases decreasing the frequency, as shown in Figs. 9k-s. In these figures, referring to one forcing cycle, the impacts are highlighted with vertical red bands. It can be observed that for f_3 (Figs. 9m,p,s), the mass impact each bumper twice, with both the intensity and duration of the second impact lower than the first one. Passing to f_2 (Figs. 9l,o,r), the mass continues to impact each bumper twice, but the second impact is more evident. Actually, also a third slight impact was sometimes observed. Finally, in correspondence to f_1 (Figs. 9k,n,q), the mass impacts, in an evident way, each bumper three times, with the intensity of the impact decreasing passing from the first one to the third one. Also in this case, sometimes four impacts were observed. This trend of the number of impacts with decreasing frequency confirms the numerical predictions [68].

5. Numerical Modeling

The numerical model of the vibro-impact system shown in Fig. 1 is illustrated in Fig. 10. In this model the behaviors of both the damper (D) and the bumpers (B_j, j = R, L) were linearized. In particular, in both cases, the resisting forces were modeled by a linear spring, with stiffness K and K_j (j = R, L) respectively, in parallel with a linear viscous damper, with damping coefficient C and C_j (j = R, L) respectively. Despite this linearization, the model is still nonlinear, due to the other sources of nonlinearity taken into account, namely the presence of the gap, the unilateral constrains and the occurrence of impact that causes abrupt changes of both stiffness and damping. For this reason, this model was called Simplified Nonlinear Model (SNM) [68]. The authors, aware of the limitations of the linear viscoelastic model, particularly when used to model the contact, consider it satisfactory for their purposes.

During its motion, the mass M can be or not in contact with the bumpers. The two conditions will be referred to as *contact* and *flight* phases respectively. The equations that govern the motion of the system are written as:

$$\begin{cases} M\ddot{u}(t) + C\dot{u}(t) + Ku(t) + F_j(t) \cdot \psi_1\left[G_j(t)\right] \cdot \psi_2\left[F_j(t)\right] \\ \qquad\qquad = -MA_t(t) \\ F_i(t) = 0 \end{cases} \tag{2}$$

where it is assumed that whether j = L then i = R, or whether j = R then i = L.

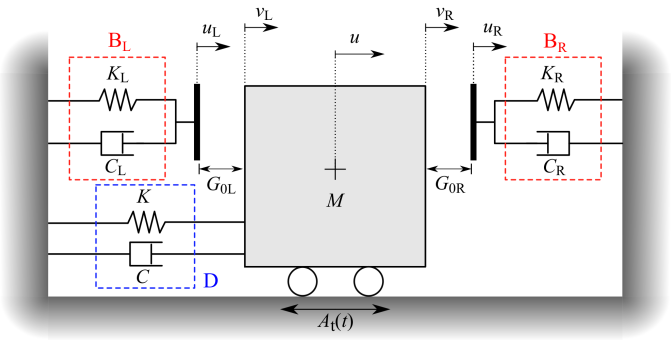

Figure 10: Numerical model of the vibro-impact system.

In Eq. 2, $u(t)$ and $u_j(t)$ (j = R, L) represent the relative displacements of the mass and of the bumpers respectively with respect to the ground and the dot $\dot{(\cdot)}$ denotes differentiation with respect to the time t. As previously said, the position of the extremity of the bumper v_j (j = R, L), measured from the side of the mass at time t = 0 s (Fig. 10), is related to u_j through the expression $v_j = u_j + G_{0j}$, where G_{0j} (j = R, L) is the j-th initial gap, that is the initial distance between the mass and the j-th bumper. $A_t(t) = A_G \sin \Omega t$ is the base acceleration, with amplitude A_G and circular frequency Ω. The total (or absolute) acceleration of the mass is therefore given by $a(t) = \ddot{u}(t) + A_t(t)$. $G_j(t)$ (j = R, L) is the clearance function which represents the distance, instant by instant, between the mass and the j-th bumper:

$$G_j(t) = G_{0j} + \Delta u_j(t) \quad (j = \mathrm{R}, \mathrm{L}) \tag{3}$$

where:

$$\Delta u_\mathrm{R}(t) = u_\mathrm{R}(t) - u(t); \;\; \Delta u_\mathrm{L}(t) = u(t) - u_\mathrm{L}(t) \tag{4}$$

When the mass is in contact with the j-th bumper $G_j(t) = 0$, otherwise $G_j(t) > 0$. In Eq. 2, ψ_1 and ψ_2 represent the Heaviside functions, defined as follows:

Beginning of the contact :

$$\psi_1\left[G_j(t)\right] = \begin{cases} 0, & G_j(t) > 0 \\ 1, & G_j(t) = 0 \end{cases}$$

Detachment :

$$\psi_2\left[F_j(t)\right] = \begin{cases} 0, & F_j(t) \le 0 \; (j = \mathrm{R}) \text{ or } F_j(t) \ge 0 \; (j = \mathrm{L}) \\ 1, & F_j(t) > 0 \; (j = \mathrm{R}) \text{ or } F_j(t) < 0 \; (j = \mathrm{L}) \end{cases}$$

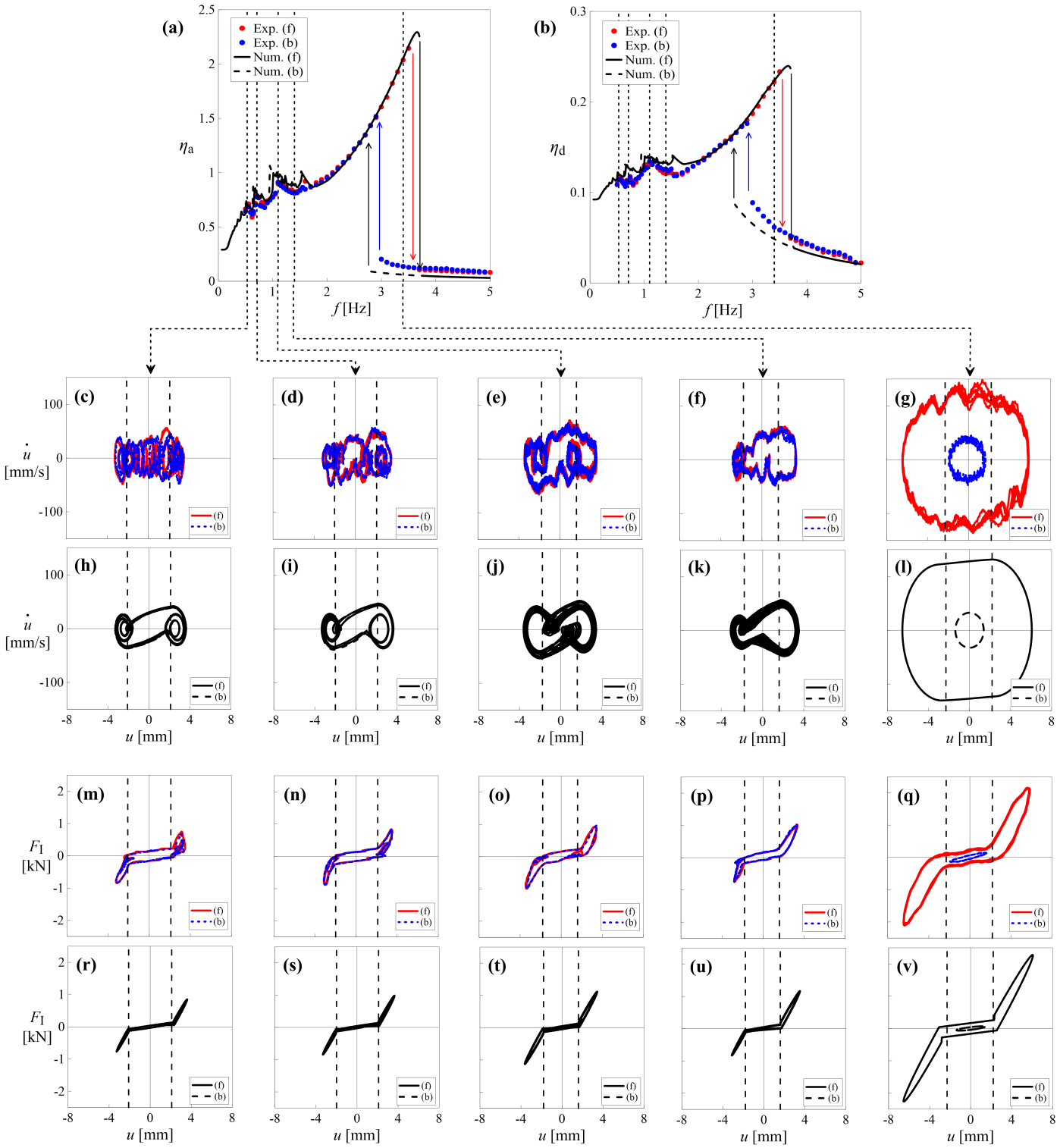

Figure 11: PRCs of **a** η_a and **b** η_a obtained experimentally (red and blue dots) and with the numerical model (solid and dashed black lines) for G4. The figures in the lower part show, for five values of frequency, namely f = 0.53 Hz, 0.71 Hz, 1.1 Hz, 1.4 Hz and 3.4 Hz, the comparison between experimental (red and blue lines) and numerical results (black lines) in terms of: trajectories on the phase plane (**c-l**); inertia force F_I vs. relative displacement u cycles (**m-v**). In **c-v** the vertical dashed black lines represent the initial gap.

where $F_j(t) = C_j\dot{u}_j(t) + K_j u_j(t)$ (j = R, L) is the contact force occurring during the contact period with the j-th bumper.

The parameters of the model were identified based on the experimental results. In order to make a comparison with the results obtained with the SNM, it was necessary to reduce the nonlinear restoring force exerted by the damper to a linear elas-

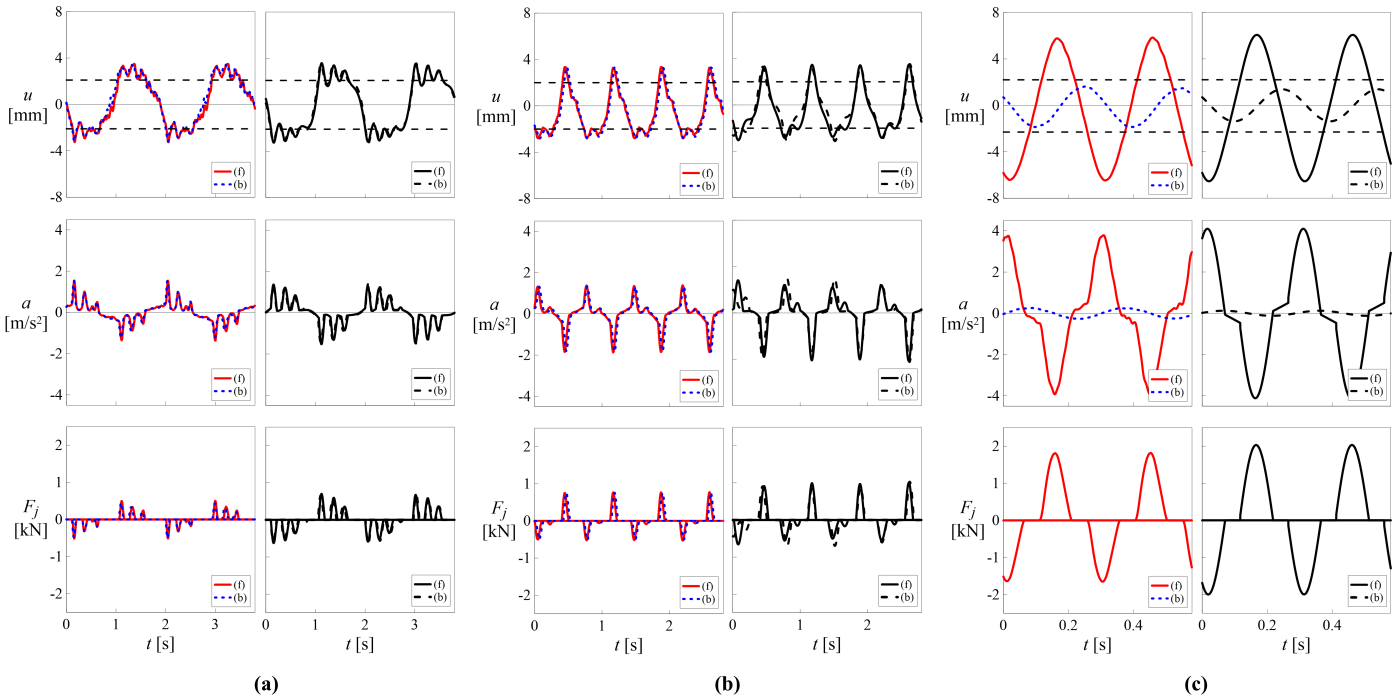

Figure 12: Time histories of the relative displacement u of the mass, the absolute acceleration a of the mass and the contact forces F_j (j = R, L) obtained experimentally (red and blue lines) and with the numerical model (black lines) for G4 and: **a** f = 0.53 Hz, **b** f = 1.4 Hz and **c** f = 3.4 Hz. The horizontal dashed black lines in the time histories of the relative displacement represent the initial gap.

tic one. This was made considering an equivalent stiffness K, estimated in free flight resonance condition for a peak table acceleration A = 0.05 g. The identified parameters of the model are: K = 36 kN/m, C = 1.1 kN s/m, for what concerns the damper, and K_j = 510 kN/m, C_j = 0.9 kN s/m, for what concerns the bumper B2 (j = R, L).

Considering the gap amplitude G4, some comparisons of the experimental results with the numerical simulations are shown in Fig. 11. In the upper part of the figure, the comparison is made in terms of PRCs of both η_a (Fig. 11a) and η_d (Fig. 11b). The experimental results are represented with red (forward sweep) and blue (backward sweep) dots, while the numerical results are represented with solid (forward sweep) and dashed (backward sweep) black lines. The vertical dashed lines indicates some values of frequency, namely 0.53 Hz, 0.71 Hz, 1.1 Hz, 1.4 Hz and 3.4 Hz, for which the comparison is made, in the lower part of Fig. 11, also in terms of phase portraits and hysteresis loops. In particular, each column of sub-figures corresponds to a frequency value. In these sub-figures, the experimental results are represented with solid red (forward sweep) and dashed blue (backward sweep) lines, while the numerical results are represented with solid (forward sweep) and dashed (backward sweep) black lines. The initial gap is represented with vertical dashed lines.

As concerns the PRCs (Figs. 11a,b), it can be observed that there is a good agreement between experimental and numerical results, although the model does not take into account nonlinearities associated with the behaviors of the damper and the bumpers. The model is able to reproduce satisfactorily the position and amplitude of both the primary resonance and some of the secondary resonances in the low frequency range. Some differences are noted in the branches of the PRCs associated with the absence of impact (after the downward jump in the forward sweep and before the upward jump in the backward sweep) and in the frequency of the upward jump. This is due to the difference between the experimental (nonlinear) and numerical (linear) PRCs in free flight condition; in particular, the numerical curve is below the experimental one. A good agreement is observed also in the trajectories on the phase plane (Figs. 11c-l) and in the force-displacement cycles (Figs. 11m-v). The presence of internal loops, whose number increases as the frequency decreases, is confirmed also by the model.

The numerical model highlighted the existence of several secondary resonances, of different type (with left hysteresis and of non-regular type), in the low frequency range (Figs. 11a,b). The calibration of the characteristics of the sine sweep signal, bound by the limitations of the shaking table, has made it possible to observe also experimentally some secondary resonances (Sect. 4.3), but not the left hysteresis, due to the limitations of the shaking table, which didn't allowed to further reduce the frequency step of the sine sweep signal. Thanks to the model it is possible to better describe what was observed with the experimentation.

From Figs. 11h-j it can be observed that, at the secondary resonances observed experimentally, the numerical response is slightly quasi-periodic, with the extent of the quasi-periodicity increasing with the frequency. Furthermore, the number of internal loops on the left is greater than that of the internal loops on the right. While the larger loops cross the vertical lines representing the obstacles in an evident way, the innermost loops

on the left as time goes by, approach, cross and then move away from the left bumper, resulting in a different number of impacts. This behavior was observed also experimentally. The situation returns to be quite symmetric, although with a greater quasi-periodicity, for $f = 1.1$ Hz (third column, Figs. 11e,j,o,t).

As previously said, the numerical model highlighted also the existence of irregularities between 1 Hz and 1.5 Hz (Figs. 11a,b). In this frequency range, an evident asymmetric response was observed experimentally, for example for $f = 1.4$ Hz (fourth column, Figs. 11f,k,p,u), and also confirmed by the numerical model. In both the phase portraits (Fig. 11f) and the hysteresis loop (Fig. 11p) a single internal loop, intersecting the left vertical dashed line (left bumper) was noticed. This results in a different number of impacts between the mass and the bumpers. In particular, in each forcing cycle, the mass impacts the left bumper twice and the right bumper once.

The asymmetric behavior of the system in this frequency range can be seen also from Fig. 12b, in which the time histories of the relative displacement u of the mass, the absolute acceleration a of the mass and the contact forces F_j (j = R, L) obtained experimentally (red and blue lines) and with the numerical model (black lines) are compared. In Fig. 12a an analogous comparisons is made for $f = 0.53$ Hz, that is in correspondence with the smallest secondary resonance observed experimentally, where the highest number of impact was observed. Finally, in Figs. 11g,l,q,v and 12c the comparison is made for a value of frequency, $f = 3.4$ Hz, that is in the frequency range between the two jumps (primary right hysteresis).

Based on these considerations, the SNM, despite its relative simplicity, has proven to be able to simulate and reproduce satisfactorily the behavior of the system.

6. Conclusions and Future Developments

Some of the results of an experimental laboratory campaign, designed based on the results of previous studies of the authors, were presented. Compared to previous tests, also small positive, null and negative values of the total gap G between mass and bumpers were investigated. Furthermore, impact load cells were used to directly measure the contact forces between mass and bumpers during the impact phases.

The amplitude of the gap was found to influence the response of both the mass and the bumpers for G > 0, where the occurrence of impact causes a hardening-like behavior, characterized by the presence of jumps and a *primary right hysteresis* in the PRCs. Referring to the primary resonance condition, the reduction of the gap, causes the reduction of the relative displacement of the mass and an increase, followed by a decrease, of the absolute acceleration. A trend similar to the latter one was observed also in the deformation of the bumpers and in the impact force, which attain zero values in the absence of impact.

By putting the bumpers initially, more or less, in contact with the mass (G $\simeq$ 0) the situation returns to be smooth, without jumps and hysteresis, although the behavior is still nonlinear, due not only to the nonlinear behaviors of the damper and the bumpers but also to the nonlinearity associated with the occurrence of impact, consequent to the existence, also in this case, of a short time interval in which the mass is in contact with either bumper.

For small negative gaps (G-1), obtained experimentally by slightly compressing the bumpers against the mass, both the relative displacement and the absolute acceleration of the mass, the bumpers' deformation and the contact force, in resonance condition, continue to decrease. Compared to G > 0, a softening-like behavior was observed, characterized by the occurrence of jumps and a *primary left hysteresis*. Furthermore, due to the initial pre-stress/pre-strain state resulting from the negative gap, the PRCs of both the bumpers' deformation and the contact forces are always different from zero for each frequency value. The transition from the hardening-like to the softening-like behavior occurs moving from small positive to negative values of the gap, passing through the approximately zero-gap configuration, not easy to realize experimentally. Compared to the case of small positive gaps (hardening) for which the increase in stiffness is caused by the occurrence of impact between the mass and one of the two bumpers, for small negative gaps (softening) the stiffness reduction is due, in a dual manner, to the detachment with one of the bumpers.

For negative gaps exceeding a certain value which, for bumper B2, is between G-1 and G-2, the mass, during its motion, always remains in contact with both bumpers and therefore, the resisting force is given by the sum of the forces exerted by the damper and the two bumpers. Consequently, the PRCs are no longer bent and show neither jumps nor hysteresis. In this case, further increases in the absolute value of the negative gap, will only increase the initial pre-stress and pre-strain state of the bumpers, without affecting the mass response.

Previous numerical investigations [68] highlighted the existence of secondary resonances, of different type (with left hysteresis and of non-regular type), in the low frequency range and for quite small gaps. Some of these resonances were observed also experimentally and the number of secondary resonances was found to increase decreasing G. To experimentally capture, in a sufficiently accurate manner, these resonances, not observed in previous experimental laboratory campaigns, it was necessary to properly calibrate the input signal, compatibly with the shaking table performances. In correspondence with the observed resonances, the occurrence of internal loops, intersecting the obstacles, in both the force-displacement cycles, rarely shown in literature, and the phase portraits, was observed. Decreasing the frequency, the number of internal loops increases, and consequently also the number of impacts per forcing cycle between the mass and the bumpers.

The experimental results were reproduced, in a sufficiently accurate manner, by a suitable numerical model, in which the behavior of both the damper and the bumpers was linearized, retaining the other sources of nonlinearities, namely the presence of the gap, the unilateral constrains and the occurrence of impact that causes abrupt changes of both stiffness and damping. The identification of the parameters of the model was made based on the experimental data. A good agreement was observed in terms of PRCs, trajectories on the phase plane, force-displacement cycles and time histories.

With regard to the future developments of this work, the au-

thors intend to finish processing the recorded data and to extend the experimental laboratory campaign also considering the earthquake excitation.

Funding This work was supported by the Great Research project of "Sapienza" University of Rome "Vibration mitigation via advanced engineered devices and materials" [N° RG11916B8160BCCC]; and "Sapienza" University of Rome [grant number RM11715C8262BE71].

Conflict of interest The authors declare that they have no conflict of interest.

References

[1] E. G. Dimitrakopoulos, Nonsmooth analysis of the impact between successive skew bridge-segments, Nonlinear Dyn. 74 (4) (2013) 911–928. doi:10.1007/s11071-013-1012-7.

[2] X. D. Gu, Z. C. Deng, Dynamical analysis of vibro-impact capsule system with Hertzian contact model and random perturbation excitations, Nonlinear Dyn. 92 (4) (2018) 1781–1789. doi:10.1007/s11071-018-4161-x.

[3] Y. Liu, M. Wiercigroch, E. Pavlovskaia, Z. Peng, Forward and backward motion control of a vibro-impact capsule system, Int. J. Non. Linear. Mech. 70 (2015) 30–46. doi:10.1016/j.ijnonlinmec.2014.10.009.

[4] Y. Liu, E. Pavlovskaia, M. Wiercigroch, Experimental verification of the vibro-impact capsule model, Nonlinear Dyn. 83 (1-2) (2016) 1029–1041. doi:10.1007/s11071-015-2385-6.

[5] Y. Yan, Y. Liu, M. Liao, A comparative study of the vibro-impact capsule systems with one-sided and two-sided constraints, Nonlinear Dyn. 89 (2) (2017) 1063–1087. doi:10.1007/s11071-017-3500-7.

[6] Y. Yan, Y. Liu, L. Manfredi, S. Prasad, Modelling of a vibro-impact self-propelled capsule in the small intestine, Nonlinear Dyn. 96 (1) (2019) 123–144. doi:10.1007/s11071-019-04779-z.

[7] L. P. de Moraes, M. A. Savi, Drill-string vibration analysis considering an axial-torsional-lateral nonsmooth model, J. Sound Vib. 438 (2019) 220–237. doi:10.1016/j.jsv.2018.08.054.

[8] S. Divenyi, M. A. Savi, M. Wiercigroch, E. Pavlovskaia, Drill-string vibration analysis using non-smooth dynamics approach, Nonlinear Dyn. 70 (2) (2012) 1017–1035. doi:10.1007/s11071-012-0510-3.

[9] M. Liao, Y. Liu, J. Páez Chávez, A. S. Chong, M. Wiercigroch, Dynamics of vibro-impact drilling with linear and nonlinear rock models, Int. J. Mech. Sci. 146-147 (2018) 200–210. doi:10.1016/j.ijmecsci.2018.07.039.

[10] X. Liu, N. Vlajic, X. Long, G. Meng, B. Balachandran, Nonlinear motions of a flexible rotor with a drill bit: Stick-slip and delay effects, Nonlinear Dyn. 72 (1-2) (2013) 61–77. doi:10.1007/s11071-012-0690-x.

[11] X. Liu, N. Vlajic, X. Long, G. Meng, B. Balachandran, Coupled axial-torsional dynamics in rotary drilling with state-dependent delay: stability and control, Nonlinear Dyn. 78 (3) (2014) 1891–1906. doi:10.1007/s11071-014-1567-y.

[12] Y. Liu, J. Páez Chávez, R. De Sa, S. Walker, Numerical and experimental studies of stickslip oscillations in drill-strings, Nonlinear Dyn. 90 (4) (2017) 2959–2978. doi:10.1007/s11071-017-3855-9.

[13] V. Vaziri, M. Kapitaniak, M. Wiercigroch, Suppression of drill-string stick-slip vibration by sliding mode control: Numerical and experimental studies, Eur. J. Appl. Math. 29 (5) (2018) 805–825. doi:10.1017/S0956792518000232.

[14] R. S. Jangid, J. M. Kelly, Base isolation for near-fault motions, Earthq. Eng. Struct. Dyn. 30 (5) (2001) 691–707. doi:10.1002/eqe.31.

[15] J. M. Kelly, Base Isolation: Linear Theory and Design, Earthq. Spectra 6 (2) (1990) 223–244. doi:10.1193/1.1585566.

[16] J. M. Kelly, The role of damping in seismic isolation, Earthq. Eng. Struct. Dyn. 28 (1) (1999) 3–20. doi:10.1002/(SICI)1096-9845(199901)28:1¡3::AID-EQE801¿3.0.CO;2-D.

[17] B. L. Su, G. Ahmadi, I. G. Tadjbakhsh, Comparative study of base isolation systems, J. Eng. Mech. 115 (9) (1989) 1976–1992.

[18] R. Jankowski, K. Wilde, Y. Fujino, Reduction of pounding effects in elevated bridges during earthquakes, Earthq. Eng. Struct. Dyn. 29 (2) (2000) 195–212. doi:10.1002/(SICI)1096-9845(200002)29:2<195::AID-EQE897>3.0.CO;2-3.

[19] A. X. Guo, Z. J. Li, H. Li, J. P. Ou, Experimental and analytical study on pounding reduction of base isolated highway bridges using MR dampers, Earthq. Eng. Struct. Dyn. 38 (11) (2009) 1307–1333. doi:10.1002/eqe.903.

[20] H. Hao, K. Bi, N. Chouw, W. X. Ren, State-of-the-art review on seismic induced pounding response of bridge structures, J. Earthq. Tsunami 7 (3) (2013) 1–19. doi:10.1142/S179343111350019X.

[21] M. Kumar, A. S. Whittaker, On the calculation of the clearance to the hard stop for seismically isolated nuclear power plants, in: Trans. 23rd Conf. Struct. Mech. React. Technol., Vol. 5, Manchester, United Kingdom, 2015.

[22] A. Sarebanha, G. Mosqueda, M. K. Kim, J. H. Kim, Seismic response of base isolated nuclear power plants considering impact to moat walls, Nucl. Eng. Des. 328 (2018) 58–72. doi:10.1016/j.nucengdes.2017.12.021.

[23] C. Alhan, H. P. Gavin, Reliability of base isolation for the protection of critical equipment from earthquake hazards, Eng. Struct. 27 (9) (2005) 1435–1449. doi:10.1016/j.engstruct.2005.04.007.

[24] M. Ismail, J. Rodellar, F. Ikhouane, An innovative isolation bearing for motion-sensitive equipment, J. Sound Vib. 326 (3-5) (2009) 503–521. doi:10.1016/j.jsv.2009.06.022.

[25] L. Y. Lu, G. L. Lin, Predictive control of smart isolation system for precision equipment subjected to near-fault earthquakes, Eng. Struct. 30 (11) (2008) 3045–3064. doi:10.1016/j.engstruct.2008.04.016.

[26] A. Reggio, M. De Angelis, Optimal design of an equipment isolation system with nonlinear hysteretic behavior, Earthq. Eng. Struct. Dyn. 42 (2013) 1907–1930. doi:10.1002/eqe.2304.

[27] A. Reggio, M. De Angelis, Combined primary-secondary system approach to the design of an equipment isolation system with High-Damping Rubber Bearings, J. Sound Vib. 333 (9) (2014) 2386–2403. doi:10.1016/j.jsv.2013.12.006.

[28] M. Basili, M. De Angelis, Optimal passive control of adjacent structures interconnected with nonlinear hysteretic devices, J. Sound Vib. 301 (1-2) (2007) 106–125. doi:10.1016/j.jsv.2006.09.027.

[29] M. Basili, M. De Angelis, A reduced order model for optimal design of 2-mdof adjacent structures connected by hysteretic dampers, J. Sound Vib. 306 (1-2) (2007) 297–317. doi:10.1016/j.jsv.2007.05.012.

[30] V. Crozet, I. Politopoulos, T. Chaudat, Shake table tests of structures subject to pounding, Earthq. Eng. Struct. Dyn. 48 (10) (2019) 1156–1173. doi:10.1002/eqe.3180.

[31] S. A. Anagnostopoulos, Pounding of buildings in series during earthquakes, Earthq. Eng. Struct. Dyn. 16 (3) (1988) 443–456. doi:10.1002/eqe.4290160311.

[32] P. C. Polycarpou, P. Komodromos, Numerical investigation of potential mitigation measures for poundings of seismically isolated buildings, Earthq. Struct. 2 (1) (2011) 1–24. doi:10.12989/eas.2011.2.1.001.

[33] P. C. Polycarpou, P. Komodromos, A. C. Polycarpou, A nonlinear impact model for simulating the use of rubber shock absorbers for mitigating the effects of structural pounding during earthquakes, Earthq. Eng. Struct. Dyn. 42 (1) (2013) 81–100. doi:10.1002/eqe.2194.

[34] A. Arena, W. Lacarbonara, A. Casalotti, Payload oscillations control in harbor cranes via semi-active vibration absorbers: Modeling, simulations and experimental results, Procedia Eng. 199 (2017) 501–509. doi:10.1016/j.proeng.2017.09.136.

[35] M. Basili, M. De Angelis, G. Fraraccio, Shaking table experimentation on adjacent structures controlled by passive and semi-active MR dampers, J. Sound Vib. 332 (13) (2013) 3113–3133. doi:10.1016/j.jsv.2012.12.040.

[36] H. P. Gavin, A. Zaicenco, Performance and reliability of semi-active equipment isolation, J. Sound Vib. 306 (1-2) (2007) 74–90. doi:10.1016/j.jsv.2007.05.039.

[37] E. Renzi, M. De Angelis, Optimal semi-active control and non-linear dynamic response of variable stiffness structures, J. Vib. Control 11 (10) (2005) 1253–1289. doi:10.1177/1077546305054597.

[38] B. Blazejczyk-Okolewska, K. Czolczynski, T. Kapitaniak, Dynamics of a two-degree-of-freedom cantilever beam with impacts, Chaos, Solitons and Fractals 40 (4) (2009) 1991–2006. doi:10.1016/j.chaos.2007.09.097.

[39] P. J. Christopher, B. Dobson, N. A. Alexander, Exploring the Dynamics of Base-Excited Structures Impacting a Rigid Stop, Math. Probl. Eng. 2020 (2020). doi:10.1155/2020/6721025.

[40] D. Costa, V. Vaziri, M. Kapitaniak, S. Kovacs, E. Pavlovskaia, M. A. Savi, M. Wiercigroch, Chaos in impact oscillators not in vain: Dynamics of new mass excited oscillator, Nonlinear Dyn. (2020). doi:10.1007/s11071-020-05644-0.

[41] H. Gritli, S. Belghith, Diversity in the nonlinear dynamic behavior of a one-degree-of-freedom impact mechanical oscillator under OGY-based state-feedback control law: Order, chaos and exhibition of the border-collision bifurcation, Mech. Mach. Theory 124 (2018) 1–41. doi:10.1016/j.mechmachtheory.2018.02.001.

[42] H. Gritli, Robust master-slave synchronization of chaos in a one-sided 1-DoF impact mechanical oscillator subject to parametric uncertainties and disturbances, Mech. Mach. Theory 142 (2019). doi:10.1016/j.mechmachtheory.2019.103610.

[43] J. Ing, E. Pavlovskaia, M. Wiercigroch, Dynamics of a nearly symmetrical piecewise linear oscillator close to grazing incidence: Modelling and experimental verification, Nonlinear Dyn. 46 (3) (2006) 225–238. doi:10.1007/s11071-006-9045-9.

[44] J. Ing, E. Pavlovskaia, M. Wiercigroch, S. Banerjee, Experimental study of impact oscillator with one-sided elastic constraint, Philos. Trans. R. Soc. A Math. Phys. Eng. Sci. 366 (1866) (2008) 679–704. doi:10.1098/rsta.2007.2122.

[45] H. Jiang, A. S. Chong, Y. Ueda, M. Wiercigroch, Grazing-induced bifurcations in impact oscillators with elastic and rigid constraints, Int. J. Mech. Sci. 127 (2017) 204–214. doi:10.1016/j.ijmecsci.2017.02.001.

[46] G. W. Luo, X. F. Zhu, Y. Q. Shi, Dynamics of a two-degree-of freedom periodically-forced system with a rigid stop: Diversity and evolution of periodic-impact motions, J. Sound Vib. 334 (2015) 338–362. doi:10.1016/j.jsv.2014.08.029.

[47] X. Lyu, Q. Gao, G. Luo, Dynamic characteristics of a mechanical impact oscillator with a clearance, Int. J. Mech. Sci. 178 (2020) 105605. doi:10.1016/j.ijmecsci.2020.105605.

[48] E. Pavlovskaia, J. Ing, M. Wiercigroch, S. Banerjee, Complex dynamics of bilinear oscillator close to grazing, Int. J. Bifurc. Chaos 20 (11) (2010) 3801–3817. doi:10.1142/S0218127410028069.

[49] H. Tao, J. Gibert, Periodic orbits of a conservative 2-DOF vibro-impact system by piecewise continuation: bifurcations and fractals, Nonlinear Dyn. 95 (4) (2019) 2963–2993. doi:10.1007/s11071-018-04734-4.

[50] F. Turki, H. Gritli, S. Belghith, An LMI-based design of a robust state-feedback control for the master-slave tracking of an impact mechanical oscillator with double-side rigid constraints and subject to bounded-parametric uncertainty, Commun. Nonlinear Sci. Numer. Simul. 82 (2020) 2–5. doi:10.1016/j.cnsns.2019.105020.

[51] J. Wang, Y. Shen, S. Yang, Dynamical analysis of a single degree-of-freedom impact oscillator with impulse excitation, Adv. Mech. Eng. 9 (7) (2017) 1–10. doi:10.1177/1687814017716619.

[52] M. Wiercigroch, S. Kovacs, S. Zhong, D. Costa, V. Vaziri, M. Kapitaniak, E. Pavlovskaia, Versatile mass excited impact oscillator, Nonlinear Dyn. 99 (1) (2020) 323–339. doi:10.1007/s11071-019-05368-w.

[53] S. Yin, G. Wen, J. Ji, H. Xu, Novel two-parameter dynamics of impact oscillators near degenerate grazing points, Int. J. Non. Linear. Mech. 120 (2020) 103403. doi:10.1016/j.ijnonlinmec.2020.103403.

[54] P. Komodromos, P. C. Polycarpou, L. Papaloizou, M. C. Phocas, Response of seismically isolated buildings considering poundings, Earthq. Eng. Struct. Dyn. 36 (12) (2007) 1605–1622. doi:10.1002/eqe.692.

[55] P. Komodromos, Simulation of the earthquake-induced pounding of seismically isolated buildings, Comput. Struct. 86 (7-8) (2008) 618–626. doi:10.1016/j.compstruc.2007.08.001.

[56] P. C. Polycarpou, P. Komodromos, On poundings of a seismically isolated building with adjacent structures during strong earthquakes, Earthq. Eng. Struct. Dyn. 39 (2010) 933–940. doi:10.1002/eqe.975.

[57] P. C. Polycarpou, P. Komodromos, Earthquake-induced poundings of a seismically isolated building with adjacent structures, Eng. Struct. 32 (7) (2010) 1937–1951. doi:10.1016/j.engstruct.2010.03.011.

[58] R. R. Aguiar, H. I. Weber, Impact force magnitude analysis of an impact pendulum suspended in a vibrating structure, Shock Vib. 19 (6) (2012) 1359–1372. doi:10.3233/SAV-2012-0678.

[59] T. Luo, Z. Wang, Periodically forced system with symmetric motion limiting constraints: Dynamic characteristics and equivalent electronic circuit realization, Int. J. Non. Linear. Mech. 81 (2016) 283–302. doi:10.1016/j.ijnonlinmec.2016.01.021.

[60] U. Andreaus, M. De Angelis, Nonlinear dynamic response of a base-excited SDOF oscillator with double-side unilateral constraints, Nonlinear Dyn. 84 (3) (2016) 1447–1467. doi:10.1007/s11071-015-2581-4.

[61] U. Andreaus, P. Baragatti, M. De Angelis, S. Perno, A Preliminary Experimental Study About Two-Sided Impacting SDOF Oscillator Under Harmonic Excitation, J. Comput. Nonlinear Dyn. 12 (6) (2017) 061010. doi:10.1115/1.4036816.

[62] U. Andreaus, P. Baragatti, M. De Angelis, S. Perno, Shaking table tests and numerical investigation of two-sided damping constraint for end-stop impact protection, Nonlinear Dyn. 90 (4) (2017) 2387–2421. doi:10.1007/s11071-017-3810-9.

[63] U. Andreaus, M. De Angelis, Experimental and numerical dynamic response of a SDOF vibro-impact system with double gaps and bumpers under harmonic excitation, Int. J. Dyn. Control 7 (4) (2019) 1278–1292. doi:10.1007/s40435-019-00532-x.

[64] U. Andreaus, M. De Angelis, Influence of the characteristics of isolation and mitigation devices on the response of single-degree-of-freedom vibro-impact systems with two-sided bumpers and gaps via shaking table tests, Struct. Control Heal. Monit. 27 (5) (2020) 1–21. doi:10.1002/stc.2517.

[65] G. Stefani, M. De Angelis, U. Andreaus, Experimental and numerical investigation of base isolated SDOF system impact against bumpers under harmonic base excitation, in: M. Papadrakakis, M. Fragiadakis (Eds.), Proc. 7th Int. Conf. Comput. Methods Struct. Dyn. Earthq. Eng. (COMPDYN 2019), Vol. 2, Institute of Structural Analysis and Antiseismic Research School of Civil Engineering National Technical University of Athens (NTUA) Greece, Athens, 2019, pp. 3333–3343. doi:10.7712/120119.7150.19207.

[66] G. Stefani, M. De Angelis, U. Andreaus, Experimental Dynamic Response of a SDOF Oscillator Constrained by Two Symmetrically Arranged Deformable and Dissipative Bumpers Under Harmonic Base Excitation, in: W. Lacarbonara, B. Balachandran, J. Ma, J. Tenreiro Machado, G. Stepan (Eds.), Nonlinear Dyn. Control, Springer International Publishing, Cham, 2020, pp. 119–127. doi:10.1007/978-3-030-34747-5_12.

[67] G. Stefani, M. De Angelis, U. Andreaus, Experimental and Numerical Response Analysis of a Unilaterally Constrained SDOF System Under Harmonic Base Excitation, in: A. Carcaterra, A. Paolone, G. Graziani (Eds.), Proc. XXIV AIMETA Conf. 2019. Lect. Notes Mech. Eng., Springer, Cham, 2020, pp. 1488–1497. doi:10.1007/978-3-030-41057-5_120.

[68] G. Stefani, M. De Angelis, U. Andreaus, Scenarios in the experimental response of a vibro-impact single-degree-of-freedom system and numerical simulations, Nonlinear Dyn. (2020). doi:10.1007/s11071-020-05791-4.